J. Fluid Mech. (2014), *vol.* 752, *pp.* 497–520. © Cambridge University Press 2014
doi:10.1017/jfm.2014.266

Nonlinear instability of a supersonic boundary layer with two-dimensional roughness

Olaf Marxen†, Gianluca Iaccarino and Eric S. G. Shaqfeh

Centre for Turbulence Research, Building 500, Stanford University, Stanford, CA 94305-3035, USA

(Received 15 August 2013; revised 21 February 2014; accepted 8 May 2014;
first published online 9 July 2014)

Nonlinear instability in a supersonic boundary layer at Mach 4.8 with two-dimensional roughness is investigated by means of spatial direct numerical simulations (DNS). It was previously found that an important effect of a two-dimensional roughness is to increase significantly the amplitude of two-dimensional waves downstream of the roughness in a certain frequency band through enhanced instability and transient growth, while waves outside this band are damped. Here, we investigate the nonlinear secondary instability induced by a large-amplitude two-dimensional wave, which has received a significant boost in amplitude from this additional roughness-induced amplification. Both subharmonic and fundamental secondary excitation of the oblique secondary waves are considered. We found that even though the growth rate of the secondary perturbations increases compared to their linear amplification, only in some of the cases was a fully resonant state attained by the streamwise end of the domain. A parametric investigation of the amplitude of the primary wave, the phase difference between the primary and the secondary waves, and the spanwise wavenumber has also been performed. The transient growth experienced by the primary wave was found to not influence the secondary instability for most parameter combinations. For unfavourable phase relations between the primary and the secondary waves, the phase speed of the secondary wave decreases significantly, and this hampers its growth. Finally, we also investigated the strongly nonlinear stage, for which both the primary and the subharmonic secondary waves had a comparable, finite amplitude. In this case, the growth of the primary waves was found to vanish downstream of the transient growth region, resulting in a lower amplitude than in the absence of the large-amplitude secondary wave. This feedback also decreases the amplification rate of the secondary wave.

Key words: boundary layer stability, compressible boundary layers, nonlinear instability

1. Introduction

Predicting the location of laminar–turbulent transition on the surface of a vehicle moving at supersonic or hypersonic speeds is a challenging task. For both re-entry and cruise vehicles an accurate prediction of the transition location offers the possibility

† Present address: Department of Mechanical Engineering, Imperial College London, Exhibition Road, South Kensington, London SW7 2AZ, UK. Email address for correspondence: o.marxen@imperial.ac.uk

https://doi.org/10.1017/jfm.2014.266 Published online by Cambridge University Press

to precisely define the dimensions of the thermal protection system and hence improve the respective vehicle design. The laminar–turbulent transition process can be divided into three main stages: receptivity, linear disturbance evolution, and nonlinear breakdown to turbulence. The latter may be subdivided into three substages: weakly nonlinear instability, strongly nonlinear instability, and final breakdown.

Early experiments by Van Driest & Blumer (1968) indicate that two-dimensional roughness may influence the location of boundary-layer transition. For the stage of linear stability for compressible, high-speed boundary layers with two-dimensional roughness, some investigations have been performed as explained below in § 1.1. However, both the weakly and the strongly nonlinear instability stages have not yet been investigated systematically for cases with two-dimensional roughness. These two stages will therefore be studied here by means of direct numerical simulations (DNS) with an emphasis on the weakly nonlinear stage. In order to introduce the nonlinear instability stage, § 1.2 provides a corresponding description for a flat-plate supersonic boundary layer.

1.1. *Linear boundary-layer instabilities in the presence of two-dimensional roughness*

Fujii (2006) conducted experiments on a cone at Mach 7 and found that transition can be delayed by two-dimensional roughness if the wall is strongly cooled, but that the transition location remains roughly the same or moves forward if wall cooling is only weak. Fujii (2006) also performed linear stability investigations and provided measured disturbance spectra. Marxen, Iaccarino & Shaqfeh (2010) applied linear stability theory and numerical simulations to investigate the instability of an adiabatic flat plate with two-dimensional roughness at Mach 4.8. They found that the amplification of two-dimensional waves is significantly increased for a narrow band of frequencies by the presence of a roughness in the boundary layer. Frequencies below this band are slightly damped, while higher frequencies are even strongly damped. They also found that oblique waves are only weakly affected. In the presence of a two-dimensional roughness, two-dimensional disturbances are hence expected to reach large amplitudes earlier than oblique waves. In order to physically explain their observations, Marxen *et al.* (2010) argue that the roughness increases the boundary-layer thickness, which in turn diminishes the stabilizing influence of viscosity and causes an increase in the thickness of local supersonic regions. Marxen *et al.* (2010) also observed that transient growth occurs downstream of the two-dimensional roughness element. However, the corresponding growth mechanism differs from the one active downstream of a three-dimensional roughness investigated by Reshotko & Tumin (2004). Similarly, Duan, Wang & Zhong (2013) found for an adiabatic flat plate at Mach 6 that a two-dimensional wave can be destabilized or stabilized, qualitatively confirming earlier results by Marxen *et al.* (2010). For a cone at Mach 5.85 with an adiabatic wall, Heitmann & Radespiel (2013) found by means of numerical simulations that the disturbance pressure amplitudes for a band of perturbations increase when a roughness element is present, again in accordance with the earlier findings of Marxen *et al.* (2010). Below we will consider cases in which a large-amplitude two-dimensional wave is present, since the mentioned results suggest that these are most strongly affected by the presence of two-dimensional roughness.

1.2. *Nonlinear instability of time-harmonic waves*

In the absence of streamwise streaks, the main weakly nonlinear mechanism active in a boundary layer is the unsteady secondary instability in the presence of a

https://doi.org/10.1017/jfm.2014.266 Published online by Cambridge University Press

two-dimensional or weakly oblique time-periodic perturbation. Once this primary perturbation, or wave, has reached a sufficient amplitude due to its linear amplification, the growth of highly oblique secondary waves with half the frequency (subharmonic resonance) or with the same frequency (fundamental resonance) as the primary wave may be significantly enhanced (Herbert 1988). This secondary instability is independent of the amplitude of the secondary wave, but parametrically depends on the amplitude of the primary wave. A characteristic feature of resonance is the synchronization of phase velocities: the secondary wave adjusts its phase speed to match the one of the primary wave.

Most of the previous numerical simulations of unsteady secondary instability have used the temporal approach, for example Ng & Erlebacher (1992) and Adams & Kleiser (1996), and only few were concerned with the spatial one (Eissler & Bestek 1996; Mayer, Wernz & Fasel 2011*b*). Bountin, Shiplyuk & Maslov (2008) carried out an experimental investigation.

Fedorov (2011) describes how second-mode instability waves could dominate at Mach numbers $M_\infty > 4$. The amplification for these waves peaks for vanishing spanwise wavenumbers. For a flat plate with $M_\infty = 4.5$, Kendall (1975) concluded that disturbances may be nonlinear at Reynolds numbers as low as $Re_x = 1350$. He further explained that 'transition was observed at $Re_x \simeq 1500$' (p. 295). The transition mechanism in the experiment remains unclear. For this case, Adams & Kleiser (1996) investigated the subharmonic route to transition using temporal numerical simulations, requiring the unrealistic assumption of streamwise periodicity. Based on spatial DNS, Eissler & Bestek (1996) conclude for a flat plate with $M_\infty = 4.8$ that the fundamental route may be at least equally important.

In summary, only a few investigations of secondary instability have been performed for spatially developing supersonic boundary layers. As mentioned above, none of these investigations considered a two-dimensional roughness element. It is therefore necessary to study both the subharmonic and the fundamental route to transition using spatial DNS for the case with two-dimensional roughness. Such a study will be reported here.

The paper is structured as follows. First, the governing equations for DNS are summarized and a description of the numerical method together with the boundary conditions (BC) and the roughness geometry is given (§ 2). To aid in the interpretation of disturbance evolution in particular downstream of the roughness, we apply linear stability theory to a flat plate in the absence of roughness (§ 3). A brief overview of the steady-state base flow with roughness and the corresponding primary instability is given in § 4. The nonlinear instability in the presence of two-dimensional unsteady waves for both subharmonic and fundamental resonance is treated in § 5. Results are summarized in § 6.

2. Governing equations, numerical method and geometry

2.1. *Governing equations*

The governing equations are the time-dependent three-dimensional Navier–Stokes equations in non-dimensional form for a compressible fluid. These equations are formulated for a calorically perfect gas with density ρ, temperature T, and pressure p. The velocity vector is given by $[u\,v\,w]^T$. It is a function of all three spatial dimensions $[x\,y\,z]^T$ and time t. Non-dimensionalization is mostly based on the free-stream conditions (marked by subscript ∞): a reference temperature $\tilde{T}_{ref} = (\gamma - 1)\tilde{T}_\infty$, density $\tilde{\rho}_\infty$, specific heat ratio $\gamma = \tilde{c}_p/\tilde{c}_v$, speed of sound $\tilde{c}_\infty$, thermal conductivity

https://doi.org/10.1017/jfm.2014.266 Published online by Cambridge University Press

$(Re_\infty M_\infty)$	Pr_∞	M_∞	T_S	s_R	$x_{c,R}$	h_R	l_R	κ	ω_0	η_0	γ
10^5	0.71	4.8	1.993	20.0	15.0	0.125	0.4	4000.0	48	10.4	1.4

TABLE 1. Simulation parameters. See text for definitions.

$\tilde{k}_\infty$, viscosity $\tilde{\mu}_\infty$, and a reference length $\tilde{L}_{ref}$ (all dimensional quantities are marked by a tilde). We have a Reynolds number $Re_\infty = \tilde{\rho}_\infty \tilde{c}_\infty \tilde{L}_{ref}/\tilde{\mu}_\infty$, a Prandtl number $Pr_\infty = \tilde{\mu}_\infty \tilde{c}_p/\tilde{k}_\infty$, and Sutherland's temperature $T_S = \tilde{T}_S/\tilde{T}_{ref}$.

The resulting set of equations has been given in Marxen *et al.* (2010) and shall therefore not be repeated here. In all plots shown below the velocities are normalized by the free-stream velocity $\tilde{u}_\infty = \tilde{c}_\infty M_\infty$ as this is common practice in the literature. To represent the streamwise axis, a local Reynolds number $Re_x = \sqrt{x Re_\infty M_\infty}$ will often be used.

2.2. *Numerical method, integration domains, and boundary conditions*

The basis for the numerical method is an algorithm described in Nagarajan, Lele & Ferziger (2003). Time-accurate solutions to the compressible Navier–Stokes equations are obtained using sixth-order compact finite differences in the interior of the domain with explicit third-order Runge–Kutta time stepping. For simulations of strongly nonlinear transitional stages (case *SB*, § 5.3), a fourth-order explicit Runge–Kutta time stepping has been applied. In order to remove aliasing errors from the solution, a small amount of dissipation is required. A damping term is added to the right-hand side of the x-momentum equation, which then reads:

$$\frac{\partial \rho u_i}{\partial t} + \frac{\partial}{\partial x_j}\left(\rho u_i u_j + p\delta_{ij}\right) = \frac{\partial \sigma_{ij}}{\partial x_j} - \kappa\left(\rho u_i - \overline{\rho u_i}\right), \quad i = 1. \tag{2.1}$$

In this equation, the overbar denotes a quantity filtered in the streamwise direction using a high-order compact filter in x so that only the high wavenumbers are affected. The viscous stress tensor is denoted by σ_{ij}, whereas δ_{ij} stands for the Kronecker delta and κ is a non-dimensional damping coefficient.

The equations are discretized on a structured, curvilinear grid using staggered variables. For three-dimensional simulations up to 720 CPUs were used, resulting in a computational time of approximately 0.364 s per time step for case *SB* ($NX \times MY \times KZ = 1800 \times 200 \times 160$).

Following what is common practice in nonlinear simulations of hydrodynamic stability (see for instance Eissler & Bestek 1996 and Mayer *et al.* 2011*b*), our simulations are denoted as DNS below.

We consider the flow over a flat plate (free stream $u_\infty = u(y_2) = \tilde{u}_\infty/\tilde{c}_\infty = M_\infty$) with a localized two-dimensional roughness. The same setup has been used in the numerical investigations of smooth walls by Eissler & Bestek (1996). The origin of the coordinate system is located at the leading edge of the flat plate. The computational domain is placed downstream of the leading edge. The parameters for our setup are given in table 1.

At the inflow x_1, a self-similar boundary-layer solution is prescribed while the wall BC at y_1 is adiabatic for the base flow with a no-slip condition. An isothermal wall is assumed for the disturbances. Within a certain region close to the outflow x_2 and in

https://doi.org/10.1017/jfm.2014.266 Published online by Cambridge University Press

Case	x_1	x_2	y_1	y_2	$L_z = (z_1 - z_2)$	NX	MY	KZ	LP
LINxx, S, F	1.6065	44.4465	Equation (2.2)	1.575	λ_z	1200	200	10	600
SB	1.6065	68.6865	Equation (2.2)	1.575	$4\lambda_z$	1800	200	160	600

TABLE 2. Specification of integration domains.

the free stream y_2, the solution is damped towards a laminar, self-similar state (sponge region). Periodicity in the spanwise direction with a domain width $L_z = (z_1 - z_2)$ is assumed. The parameters specifying the dimensions of the domain are given in table 2. The shape of the roughness is defined as follows:

$$y_1(x) = \frac{h_R}{2} \sum_{q=-1}^{+1} q \left(\tanh\left(s_R \left(x - x_{0,q}\right)\right) + 1\right) \quad \text{with } x_{0,q} = x_{c,R} - q l_R/2. \tag{2.2}$$

The length l_R corresponds to the distance between the two inflection points in the roughness geometry, while s_R can be considered a steepness parameter for the flank of the roughness. The centre of the roughness is located at $x_{c,R}$. We consider only a single roughness height h_R and length l_R, and the inflection points are located at $x \approx 14.8$ and $x \approx 15.2$. Figure 6 below visualizes the resulting shape of the roughness. Marxen *et al.* (2010) have varied these parameters for linear perturbations. They found that the overall effect of a two-dimensional roughness, namely lasting increase of amplitude for selected frequencies and transient growth in the vicinity of the roughness, is qualitatively independent of the length of the roughness (see figure 25 in Marxen *et al.* 2010). Moreover, the disturbance amplitude increases with roughness height, but this increase is largest for small roughness heights and then levels off (see figure 18 in Marxen *et al.* 2010). Therefore, we did not vary the length of the roughness for our investigation and picked a height which corresponds to the largest height investigated by Marxen *et al.* (2010).

The grid line $m = 1$ collapses with the wall, i.e. it follows $y_1(x)$. In the streamwise and spanwise directions, the domain is subdivided with an equidistant spacing in the x and z directions with NX and KZ points, respectively. In the wall-normal direction, we use the same grid stretching as Marxen *et al.* (2010).

2.3. *Disturbance forcing*

Disturbances of a fixed frequency are forced via blowing and suction at the wall upstream of the roughness element. The non-dimensional forcing frequency $\omega = h\omega_0$ is derived from a dimensional base frequency $\tilde{f}_0$:

$$\omega_0 = F_0 M_\infty^2 Re_\infty \quad \text{with } F_0 = 2\pi\tilde{f}_0 \left(\tilde{\mu}/(\tilde{\rho}\tilde{u}^2)\right)_\infty. \tag{2.3}$$

The BC at the wall is:

$$v^{wall} = \sum_{h=0.5,1;k=-1,0,1} A_{(h,k)} \sin(h\,\omega_0\,t + \Phi_0) \sin(16\,\xi) \exp\left(-\sqrt{2}\xi^2/2\right) \cos(k\,\eta_0\,z), \tag{2.4}$$

with $\xi = (x - x_{c,strip})/L_{strip}$, subscript *strip* denoting the forcing strip, and $\eta_0 = 2\pi/\lambda_z$, and where A is the disturbance amplitude and Φ_0 the phase. For investigations of secondary instability (§ 5), a finite-amplitude two-dimensional primary wave ($h = 1$, $k = 0$, $\Phi_{0,primary} = 0$) is forced in addition to a pair of small-amplitude oblique secondary waves. The secondary waves possess either half the frequency of the primary wave or the same frequency, and a non-zero spanwise wavenumber

https://doi.org/10.1017/jfm.2014.266 Published online by Cambridge University Press

Mode $(h, \pm k)$	$x_{c,strip}$	L_{strip}	$\omega = h\,\omega_0$	$F = h\,F_0$	$Re_{x_{c,strip}}$	$\eta = k\,\eta_0$
(1, 0)	5.49	4.203	48	1.0×10^{-4}	741	0.0
(0.5, ±1)	5.49	8.430	24	0.5×10^{-4}	741	10.4
(1, ±1)	5.49	4.203	48	1.0×10^{-4}	741	10.4

TABLE 3. Forcing parameters.

Case	(1, 0)	(0.5, ±1)	(1, ±1)	$\Phi_{0,secondary}$
LIN2D	2.5×10^{-4}	0	0	0
LIN3D-S	0	2.5×10^{-4}	0	0
LIN3D-F	0	0	2.5×10^{-4}	0
S	8.75×10^{-3}	2.5×10^{-4}	0	0
F	8.75×10^{-3}	0	2.5×10^{-4}	$\pi/2$
SB	8.75×10^{-3}	2.5×10^{-3}	0	0

TABLE 4. Disturbance amplitudes $A_{(h,k)}$ and phases $\Phi_{0,secondary}$ for all cases.

($h = 0.5$ or $h = 1$, $|k| = 1$, $\Phi_{0,secondary} = 0$ or $\Phi_{0,secondary} = \pi/2$). The phase difference between the primary and the secondary wave is fixed:

$$\Delta\Phi = \Phi_{0,primary} - \Phi_{0,secondary}. \tag{2.5}$$

Forcing parameters, including $x_{c,strip}$ and L_{strip}, for different frequencies are given in table 3, while the disturbance amplitude for different cases is specified in table 4. In case *SB*, a pair of finite-amplitude oblique waves is excited, and additional background noise is introduced by random forcing. In all cases, $A_{(0.5,0)} \equiv 0$.

The time step for all the numerical simulations was specified based on the frequency of the primary disturbance forcing ω_0:

$$\Delta t = \frac{2\pi}{\omega_0}\frac{1}{LP}, \tag{2.6}$$

with the number of time steps per forcing period LP given in table 2.

2.4. *Post-processing: Fourier analysis in time and spanwise direction*

In order to analyse the instability of the boundary layer, results are Fourier transformed in t and z with a fundamental circular frequency $\Omega_0 = \omega_0/2$. Still, the reference circular frequency for our notation is ω_0, while the fundamental spanwise wavenumber for the Fourier analysis is η_0. The notation (h, k) is used to refer to a disturbance with a frequency $h\omega_0$ and a spanwise wavenumber $k\eta_0$.

The corresponding discrete Fourier transform reads:

$$\hat{s}_{(h,k)}(x) = \frac{1}{50}\sum_{l=1}^{50}\sum_{d=1}^{KZ} s(\boldsymbol{x}, t_l)\exp\left[2\,\mathrm{i}h\,\Omega_0\,t_l\right]\exp\left[\mathrm{i}k\eta_0 z_d\right], \tag{2.7}$$

with $h = [0, 0.5, 1]$, $s = u, v, w, \rho, T, p$, where 50 samples are taken within two periods $2\pi/\omega_0$, l is the sampling index, the discrete time is $t_l = 2/50\,LP\,l\Delta t$, and the discrete spanwise coordinate is $z_d = d\Delta z$. Also, $F_0 = \omega_0(Re_\infty M_\infty^2)^{-1} = 2\Omega_0(Re_\infty M_\infty^2)^{-1}$. The Fourier coefficient $\hat{s}_{(h,k)}(\boldsymbol{x})$ is complex, with an amplitude $|\hat{s}_{(h,k)}|$ and the phase is defined as:

$$\Phi_{(h,k)} = \arctan\left(\mathrm{Im}(\hat{s}_{(h,k)})/\mathrm{Re}(\hat{s}_{(h,k)})\right). \tag{2.8}$$

https://doi.org/10.1017/jfm.2014.266 Published online by Cambridge University Press

The streamwise disturbance amplification is quantified using wall-normal maxima of the amplitudes of a disturbance quantity $\hat{s}_{(h,k)}$, which are computed as:

$$\hat{s}^{max}_{(h,k)}(x) = \max\{|\hat{s}_{(h,k)}(x = \text{const}, y)|\}. \tag{2.9}$$

The amplification rate α_i is computed from the pressure at the wall ($y = 0$):

$$\alpha_{i,(h,k)}(x) = \frac{1}{\hat{p}^{wall}_{(h,k)}} \frac{\partial \hat{p}^{wall}_{(h,k)}}{\partial x} \frac{Re_x}{Re_\infty}. \tag{2.10}$$

Unless stated otherwise, the phase velocity is computed from the pressure at the wall ($\hat{s} = \hat{p}^{wall}$ in (2.8)). Note that $c_{ph,(h,k)}$ is non-dimensionalized by the free-stream velocity, i.e. $c_{ph,(h,k)} = \tilde{c}_{ph,(h,k)}/\tilde{u}_\infty = \tilde{c}_{ph,(h,k)}/(\tilde{c}_\infty M_\infty)$:

$$c_{ph,(h,k)} = Re_\infty M_\infty h F_0 \left(\partial \Phi_{(h,k)}/\partial x\right)^{-1}. \tag{2.11}$$

2.5. *Verification*

The numerical simulation code has previously been verified. A verification for case *LIN2D* is reported in Marxen *et al.* (2010). For a chemically reacting flow with small-amplitude disturbance, a version of the code has been verified as reported in Marxen *et al.* (2011). Additional verification comes from a comparison between our results and linear stability theory, exhibiting in general good agreement as discussed in § 3.

For three-dimensional simulations without breakdown to turbulence, cases *LIN3D-S/F*, *S* and *F*, the secondary disturbance with non-zero spanwise wavenumber still behaves linearly. A low resolution of 10 spanwise grid points per wavelength was sufficient to accurately capture the disturbance evolution. This has been verified by repeating the simulation with twice the number of spanwise grid points, which gives results that are indistinguishable from the lower-resolved ones to plotting accuracy (figure 1). In the streamwise and wall-normal directions, the same discretization as for the two-dimensional cases (e.g. *LIN2D*) has been applied. Simulations of late transitional stages (case *SB*) required a higher resolution in z. The resolution for all cases is given in table 2.

In order to verify our simulation code for investigations of nonlinear instability, we have computed case F3 of Eissler & Bestek (1996), which is based on the same free-stream conditions as used in our investigations with two-dimensional roughness. In this case F3, a large-amplitude two-dimensional instability wave (figure 2*a*) induces strong amplification of a pair of oblique waves (figure 2*b*) with the same frequency due to fundamental resonance. As can be seen in figure 2, we obtain favourable agreement between our results (symbols) and those reported in Eissler & Bestek (1996), in particular in the most important region of secondary amplification ($x > 28$ in figure 2*b*). Differences are restricted to the region where the beating between modes S and F ends and the amplified mode emerges ($x \in [20, 25]$), for a definition of modes S and F see § 3. Since the amplitude of the oblique secondary waves is not exactly reported in Eissler & Bestek (1996), it has been scaled so that our results match those of Eissler & Bestek (1996) close to the strip used for disturbance excitation.

https://doi.org/10.1017/jfm.2014.266 Published online by Cambridge University Press

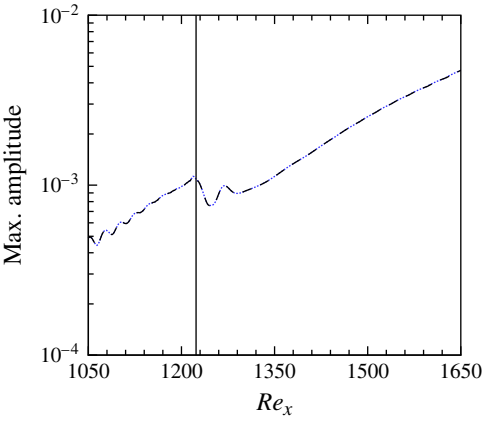


FIGURE 1. (Colour online) Amplitude $\hat{u}^{max}_{(1/2,\pm1)}$ for $h_R = 0.125$ case *S*. Results with a spanwise resolution of $KZ = 10$ (– –) and $KZ = 20$ grid points (· · ·). For a case description see § 5.1.

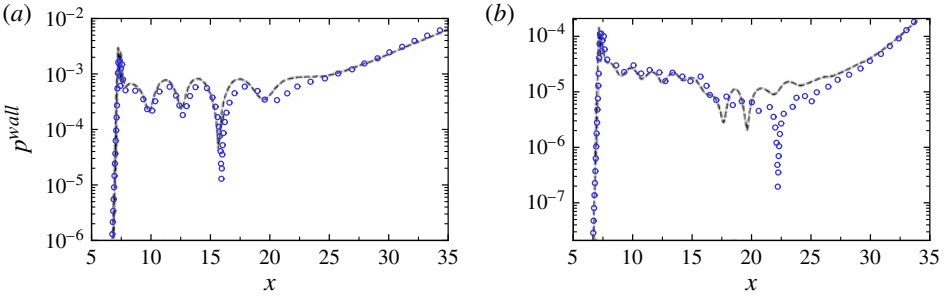


FIGURE 2. (Colour online) Amplitude $\hat{p}^{wall}_{(h,k)}$ for a flat-plate boundary layer (present results: ○) compared to the flat-plate results of Eissler & Bestek (1996), their case F3 (– –). (*a*) Mode $(h, k) = (1, 0)$ and (*b*) mode $(h, k) = (1, \pm1)$ with $\eta = 11$. Note that in our definition, Fourier amplitudes are smaller by a factor of two compared to Eissler & Bestek (1996).

3. Analysis based on linear stability theory

A spatial linear stability analysis has been performed based on the linearized compressible Navier–Stokes equations assuming parallel flow. Eigensolutions are computed by a shooting method developed and implemented by Mack (1969). For a fixed (real) frequency parameter $F = h F_0$ and a constant spanwise wavenumber $\eta = k\,\eta_0$, a single complex eigenvalue $\alpha = \alpha_r + \mathrm{i}\alpha_i$ is computed. It is composed of a streamwise wavenumber $\alpha_r = h\,\omega_0/(c_{ph}M_\infty)$ and a streamwise amplification rate α_i. Again, c_{ph} has been non-dimensionalized by the free-stream velocity, i.e. $c_{ph} = \tilde{c}_{ph}/\tilde{u}_\infty = \tilde{c}_{ph}/(\tilde{c}_\infty M_\infty)$. The scaled spanwise wavenumber β_r is defined as $\beta_r = \eta Re_x/(Re_\infty M_\infty)$.

Two eigenmodes are of particular interest in a supersonic boundary layer, commonly denoted as mode F and mode S (Fedorov 2011). A fast acoustic mode with a phase velocity of $c_{ph} = 1 + 1/M_\infty$ at the leading edge of the flat plate evolves into mode F

https://doi.org/10.1017/jfm.2014.266 Published online by Cambridge University Press

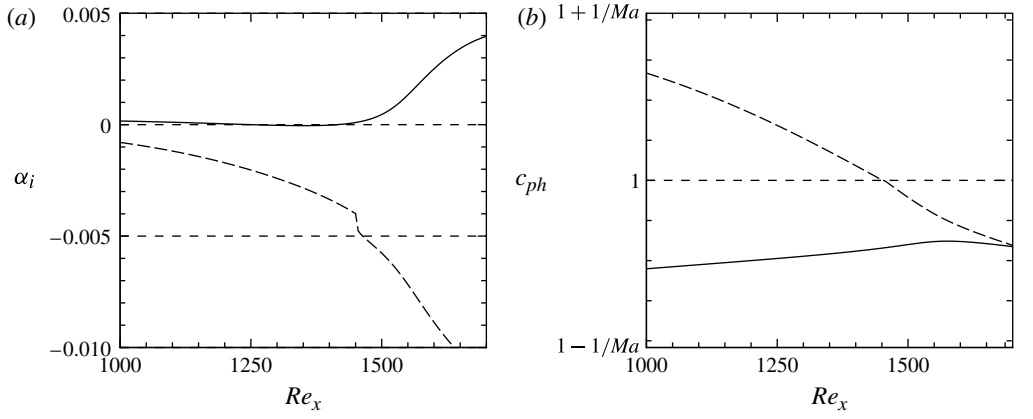


FIGURE 3. Flat-plate amplification rate (*a*) and phase velocity (*b*) from linear stability theory for a frequency $F = 1.0 \times 10^{-4}$. Results for two-dimensional ($\beta_r = 0$) eigensolutions mode S (—) and mode F (– –).

further downstream. Analogously, mode S originates from a slow acoustic mode with a phase velocity of $c_{ph} = 1 - 1/M_\infty$ at the leading edge.

For a two-dimensional disturbance ($\beta_r = 0$) in the flat-plate boundary layer under consideration here, results for the two modes are depicted in figure 3. Only mode S exhibits two regions of disturbance growth, in which the amplification rate α_i is positive. Mechanisms for disturbance growth are different in the two regions. In the instability region for $Re_x < 1300$, the instability is of the first type, caused mainly by a generalized inflection point in the boundary-layer profile (Kelvin–Helmholtz instability). In the instability region for $Re_x > 1300$, we have a second-type or Mack instability associated with trapped acoustic waves (Mack 1969).

Fedorov (2011) explains that the second-type instability begins close to the Reynolds numbers where the phase velocities of mode F and S coalesce, leading to a synchronization region. Figure 3 confirms that strong amplification of mode S occurs where the phase velocities of the two modes approach each other. According to Fedorov (2011), a local analysis may not be reliable without special procedures in the synchronization region.

For an oblique wave with half the frequency of the two-dimensional one just considered, again only mode S exhibits disturbance growth, which is of the first type. For non-zero spanwise wavenumbers, a more complete picture of the behaviour of mode S arises from the stability diagrams given in figure 4. For $F = 0.5 \times 10^{-4}$, a normalized spanwise wavenumber of $\beta_r \approx 0.1$ belongs to the most amplified disturbance, in particular when the roughness is present (figure 4*b*). In our numerical simulation, β_r cannot be kept constant. Instead, a constant physical spanwise wavenumber η results in an increase in β_r with Re_x. For the spanwise wavenumber η_0 selected for simulations here, this is indicated by the lines in figure 4. With roughness (figure 4*b*), a region of increased amplification is followed by damping so that the integral effect of a two-dimensional roughness on first-type oblique waves is small.

For a flat plate, figure 5(*a*) depicts a comparison of results from linear stability theory and numerical simulation for a two-dimensional wave. The agreement for both the phase velocity and the amplification rate is as good as that found by

https://doi.org/10.1017/jfm.2014.266 Published online by Cambridge University Press

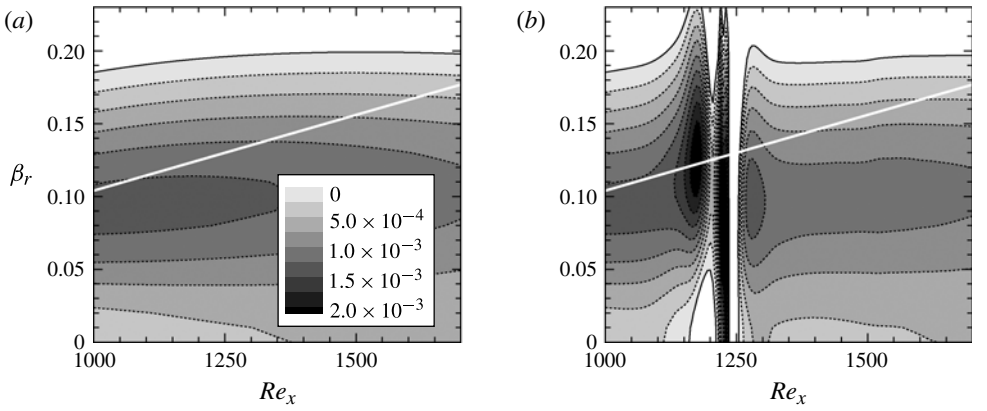


FIGURE 4. Stability diagrams (contours of the amplification rate $\alpha_i Re_x/Re_\infty$ from LST) for varying spanwise wavenumbers β_r with fixed frequency parameter $F = 0.5 \times 10^{-4}$. The white line marks the fundamental spanwise wavenumber $\eta_0 = 10.4$ used in cases *S/SB* and *LIN3D-S*, i.e. it corresponds to mode $(1/2, \pm 1)$. The contour lines span an interval 0 to 0.005, $\Delta = 0.000\,25$. (*a*) Flat plate and (*b*) with roughness ($h_R = 0.125$).

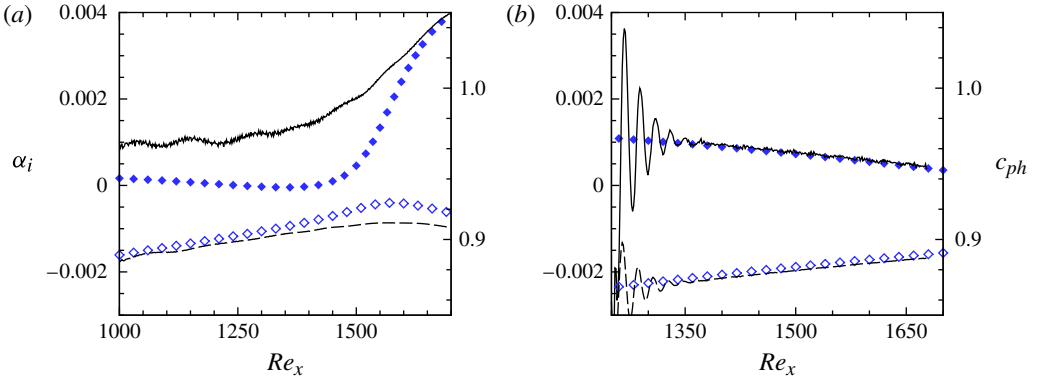


FIGURE 5. (Colour online) Comparison of results for a flat plate from DNS (lines) and LST, mode S (symbols): amplification rate α_i (—, ♦) and phase velocity c_{ph} (– –, ◇). (*a*) $(h, k) = (1, 0)$, DNS case *LIN2D* and (*b*) $(h, k) = (1/2, \pm 1)$, DNS case *LIN3D-S*.

Ma & Zhong (2003) in their case (compare, for example, their figure 19). Observable differences are likely to be connected to the assumptions made in the local linear approach. According to figure 9 in Pagella, Rist & Wagner (2002), the wall pressure exhibits a particularly large growth rate, while other quantities such as wall-distant disturbance velocity maxima may result in a better agreement. Pagella *et al.* (2002) show that non-parallel effects are responsible for the difference between theory and numerical simulation. For a similar flow case, Lifshitz, Degani & Tumin (2012) confirm that the 'discrepancy between LST and DNS results can be attributed to the nonparallel flow effects' (p. 2205).

For oblique waves, a perfect agreement for both amplification rate and phase velocity is obtained when using the wall pressure. Results for mode S depicted in figure 5(*b*) correspond to values found at the line given in figure 4(*a*). Differences are

https://doi.org/10.1017/jfm.2014.266 Published online by Cambridge University Press

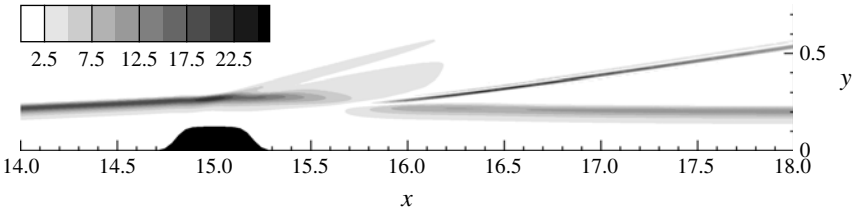


FIGURE 6. Contours of the absolute wall-normal density gradient $|\partial\rho/\partial y|$ for $h_R = 0.125$, steady-state laminar flow.

restricted to the region still influenced by the disturbance strip, i.e. for $Re_x < 1350$, where oscillations can be seen (figure 5*b*). Such a level of agreement has also been observed by Mayer, von Terzi & Fasel (2011*a*), see their figure 6.

4. Base flow and primary instability

4.1. *Steady-state laminar flow*

Only a brief overview of the unperturbed laminar flow with two-dimensional roughness is given here; more details can be found in Marxen *et al.* (2010). A representation of the flow field is given in figure 6 by means of a numerical Schlieren image. Boundary-layer separation occurs both upstream and downstream of the roughness. For $h_R = 0.125$, the ratio between the boundary-layer thickness δ_{99}, based on $\tilde{u}/\tilde{u}_\infty = 0.99$ for the flat plate at the centre location of the roughness ($x_{c,R} = 15$), and the roughness height is $h_R/\delta_{99} \approx 0.6875$.

The roughness element causes a compression followed by an expansion, which again is followed by a compression. The latter causes a weak oblique shock downstream of the roughness element, clearly visible in the region $x > 15.8$, $y > 0.2$ in figure 6. The expansion downstream of the roughness leads to an acceleration of the flow in the free stream. This acceleration causes the streamlines to turn toward the wall after they have been deflected away from the wall by the roughness. Downstream of the roughness the shock causes the streamlines to become approximately wall parallel again (Marxen *et al.* 2010).

4.2. *Primary instability*

Several aspects of the linear instability of the present flow with roughness have been discussed in Marxen *et al.* (2010), including an explanation of physical disturbance growth mechanisms. Below, complementary aspects not covered by Marxen *et al.* (2010) are presented. Only those parameters (roughness height, frequencies and wavenumbers) will be considered that are relevant for the nonlinear investigations reported later.

Marxen *et al.* (2010) observed that the roughness element creates a narrow band of frequencies in which a significant gain in amplitude over the flat-plate case is observed for two-dimensional disturbances. This feature makes the case well suited for investigations of secondary instability, since the primary disturbance is likely to have a frequency in the range experiencing additional amplification. Here, a frequency within this range, namely $F = 1 \times 10^{-4}$, is considered as the primary disturbance frequency in subsequent investigations of nonlinear disturbances. The position of the roughness relative to where mode F and mode S synchronize influences the effect of

https://doi.org/10.1017/jfm.2014.266 Published online by Cambridge University Press

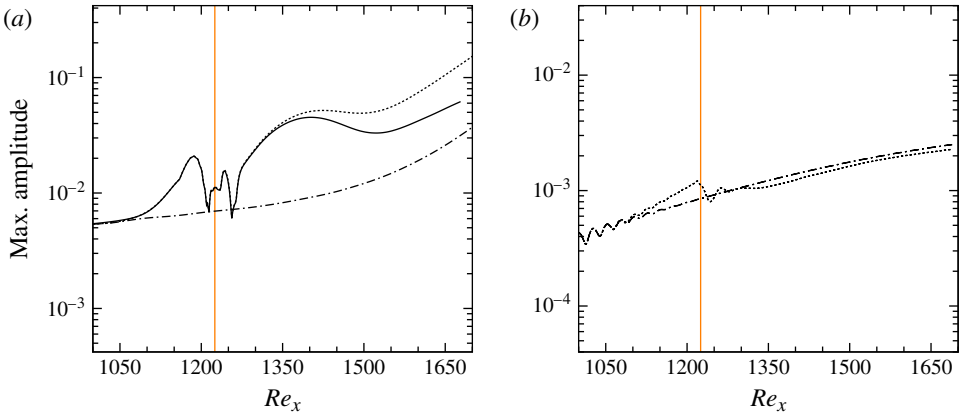


FIGURE 7. (Colour online) Amplitude $\hat{u}^{max}_{(h,k)}$ from DNS for $h_R = 0.125$ (—, · · ·) and a flat plate (– · –). The vertical lines mark the centre location of the roughness. (*a*) $(h, k) = (1, 0)$ case *F* (—) and case *LIN2D* (· · ·, – · –) and (*b*) $(h, k) = (1/2, \pm 1)$ case *LIN3D-S* (· · ·, – · –).

the roughness on disturbance amplification. Marxen *et al.* (2010) varied disturbance frequency with a fixed roughness position, whereas Duan *et al.* (2013) achieved a similar effect by varying the position of the roughness for a fixed frequency. The combination of disturbance frequency and roughness position selected here ensures that the primary wave in our study experiences a particularly strong boost in amplification.

Figure 7(*a*) compares the disturbance evolution for the streamwise velocity component for two different amplitudes for a localized two-dimensional roughness. The dash-dotted line in figure 7 belongs to a flat-plate boundary layer. The figure confirms that the roughness acts as a local growth modifier for two- (figure 7*a*) and three-dimensional (figure 7*b*) disturbances as pointed out by Marxen *et al.* (2010), leading to an increase in downstream amplitude for Fourier mode (1, 0) here.

Marxen *et al.* (2010) found that in front of and behind the roughness, additional synchronization points occur for a two-dimensional disturbance, at which modes S and F have equal phase velocities (see figure 9*a* in Marxen *et al.* 2010). As a result and possibly due to the weak shock, close to the roughness the stable mode F is excited. The superposition of modes F and S downstream of the roughness then leads to a beating: constructive (and destructive) interference occurs. This causes an oscillation of the phase velocity around the expected theoretical value (symbols), as visible at the wall (see figure 8*a*, curve for $y = 0$). This beating explains the transient growth for two-dimensional disturbances in the region $Re_x = 1300$–1400 (figure 7*a*).

For our investigations of secondary instability, we will use the results from LST for the two-dimensional wave (symbols in figure 8*a*) to determine whether resonance has occurred: for resonance, an oblique wave of fundamental or subharmonic frequency should deviate from the linear value (for subharmonic waves, see figure 8*b*) and exhibit the former phase velocity instead.

If the amplitude of the forced wave, mode (1, 0), is sufficiently large, saturation effects are observed for the two-dimensional wave, leading to a decrease in amplification rate and hence amplitude (compare the solid and the dotted line in figure 7*a*). The transient growth region $Re_x = 1300$–1400 remains almost unaffected,

https://doi.org/10.1017/jfm.2014.266 Published online by Cambridge University Press

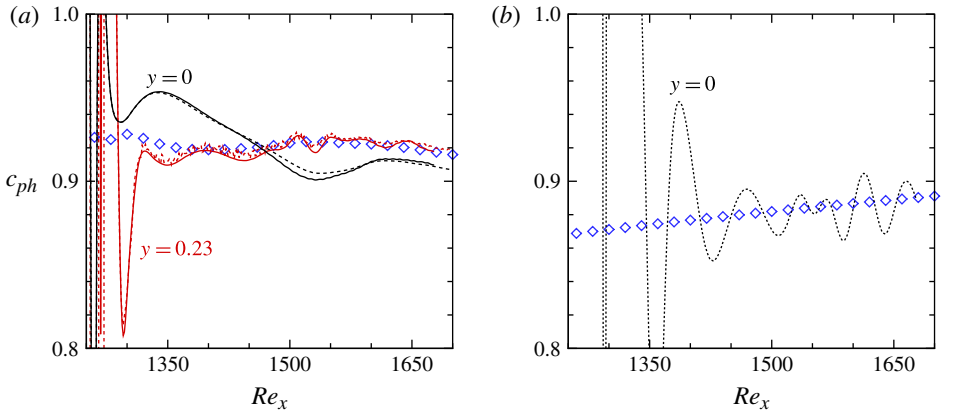


FIGURE 8. (Colour online) Phase velocity $c_{ph}^{(h,k)}$ for $h_R = 0.125$ from DNS (based on the pressure at different y-locations, as marked) and LST, mode S ($\diamond$). (*a*) $(h, k) = (1, 0)$, DNS cases *F* (—) and *LIN2D* ($\cdots$) and (*b*) $(h, k) = (1/2, \pm 1)$, DNS case *LIN3D-S* ($\cdots$).

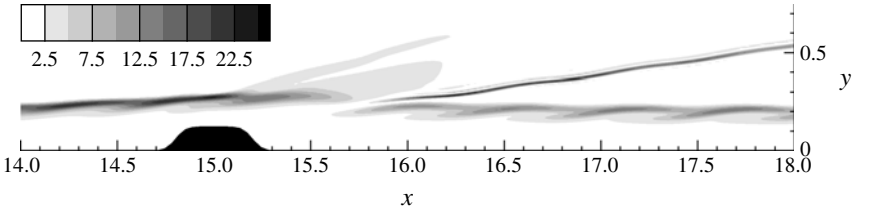


FIGURE 9. Instantaneous contours of the absolute wall-normal density gradient $|\partial\rho/\partial y|$ at $z = 0$ for $h_R = 0.125$, case *F*.

suggesting that mode F is not much affected by nonlinearity. The phase velocity remains almost the same independent of amplitude (figure 8*a*).

An instantaneous view of the large-amplitude two-dimensional wave is given in figure 9. Not only do we see a perturbation at the edge of the boundary layer, but also the oblique shock caused by the roughness exhibits oscillations. The boundary-layer edge perturbations look similar to those that Kimmel & Poggie (1997) observed experimentally on a cone (compare their figure 7).

5. Secondary instability

Using secondary stability analysis and temporal numerical simulations assuming periodicity in the streamwise direction, Ng & Erlebacher (1992) found significant secondary growth for a high-frequency primary two-dimensional disturbance, with a frequency parameter roughly twice the present one (they used a streamwise wavenumber of $\alpha_{NE92} = 2.52$ for a Reynolds number of $Re_{NE92} = 10\,000$, which would give a corresponding frequency parameter of $F_{NE92} = (\alpha_{NE92}/Re_{NE92})c_{ph} \approx 2.3 \times 10^{-4}$ if we assume a phase velocity of 0.9). However, both the secondary stability analysis and the temporal simulation method assume parallel flow. Their results may hence not be applicable to spatially developing flows, which exhibit boundary-layer growth and a corresponding change in the stability behaviour of the primary wave. Since waves

https://doi.org/10.1017/jfm.2014.266 Published online by Cambridge University Press

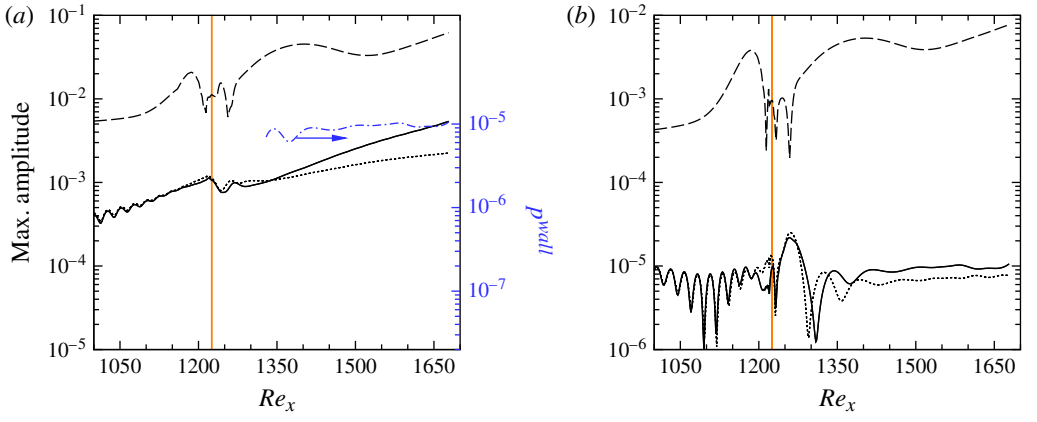


FIGURE 10. (Colour online) Amplitudes $\hat{a}_{(h,k)}$ for $h_R = 0.125$ and different modes (h, k). Case S $(1, 0)$ (– –), case S $(1/2, \pm 1)$ (—), case $LIN3D$-S $(1/2, \pm 1)$ $(\cdots)$. (a) $\hat{a} = \hat{u}^{max}$ and (b) $\hat{a} = \hat{p}^{wall}$. The centre of the roughness is marked by a vertical line.

with a high frequency are strongly damped due to the presence of a two-dimensional roughness, it is more realistic in our case S to consider a moderately high frequency.

5.1. *Weakly nonlinear results for subharmonic secondary waves*

For the same setup as our case S, including the same frequency of the primary wave, Eissler & Bestek (1996) investigated the subharmonic secondary instability for two different spanwise wavenumbers $\eta = 6.0$ and $\eta = 20.0$, albeit without a roughness. For the lower of the two wavenumbers, they did not find any significant increase in the growth rate for the disturbance pressure due to a secondary instability. Moreover, even in the case of the larger wavenumber, they found that the amplification remains below that they saw for fundamental resonance (discussed in § 5.2).

Disturbance amplification for the case of subharmonic secondary excitation, case S, is depicted in figure 10. This figure confirms that the amplification of a pair of oblique waves increases in the presence of a large-amplitude two-dimensional wave if we consider the streamwise velocity component (figure 10*a*). However, the pressure does not grow along Re_x, but rather only exhibits an elevated level if compared to the linear case (figure 10*b*). Our results for $\eta = 10.4$ are therefore very similar to the findings of Eissler & Bestek (1996), who observed growth in the streamwise velocity disturbance for $\eta = 20$. They denoted the increase in growth rate as Craik-type resonance.

It is remarkable that the local peak in primary amplitude at $Re_x = 1400$, which is associated with transient growth due to the superposition of a mode F and mode S perturbation, does not lead to a local peak in the secondary amplification rate. This suggests that the stable mode F does not contribute strongly to the secondary resonance mechanism.

A resonant interaction of the secondary wave will lead to matching phase velocities of the primary and the secondary waves. Without resonance, according to linear stability theory the two waves do not have matching phase velocities for $\eta = 10.4$ as found by Eissler & Bestek (1996) (see their figure 17*b*). This can also be seen in our simulations by comparing the dotted lines for $y = 0$ in figures 8(*a*) and 8(*b*).

https://doi.org/10.1017/jfm.2014.266 Published online by Cambridge University Press

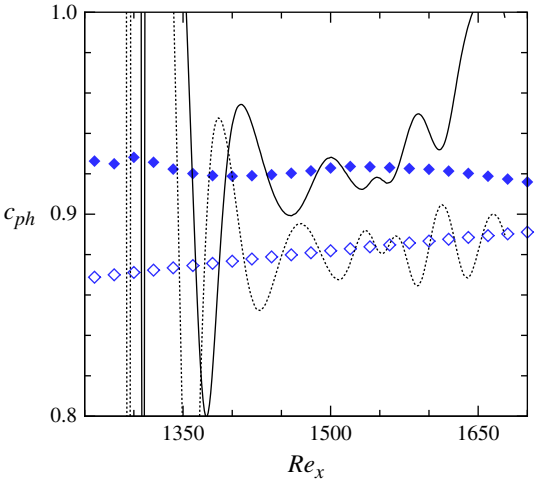


FIGURE 11. (Colour online) Phase velocity $c_{ph}^{(h,k)}$ for $h_R = 0.125$ from DNS (based on the pressure at $y = 0$) and LST, mode S. DNS mode $(h, k) = (1/2, \pm 1)$ from cases *S* (—) and *LIN3D-S* ($\cdots$), and LST mode $(h, k) = (1, 0)$ (♦) and mode $(h, k) = (1/2, \pm 1)$ (◇).

Therefore, the oblique waves have to adjust their phase speed in order to fall into resonance with the two-dimensional wave. Such an adjustment can be confirmed here by looking at the phase velocity for case *S* (figure 11). For zero amplitude of the two-dimensional wave, the DNS result for the oblique waves follows the result from linear stability theory as could be seen in figure 8(*b*), and is repeated here for convenience: compare the dotted line with the open diamonds in figure 11. In the presence of a large-amplitude two-dimensional wave, however, the phase velocity of the oblique waves adjusts itself to match the phase velocity of the two-dimensional wave (compare the solid line with the filled diamonds in figure 11). Downstream of $Re_x \approx 1600$ the phase speed of the oblique waves in case *S* increases further, but the reason for this increase is not known.

5.1.1. *Influence of the amplitude of the primary wave*

In order to investigate the effect of the amplitude of the primary wave, a range of values for this amplitude has been considered. The simulations are the same as those for case *S*, except that the forcing amplitude of mode (1, 0), $A_{(1,0)}$, has been varied. The result depicted in figure 10, i.e. case *S*, corresponds to the largest amplitude considered, in which case a significant increase of $\hat{u}$-amplification could be observed. For the smallest amplitude considered, for which $A_{(1,0)} = 0.125 \times 10^{-2}$, the primary disturbance had a small damping effect. This effect was even more pronounced for an intermediate amplitude (figure 12*a*) with $A_{(1,0)} = 0.39 \times 10^{-2}$.

The reason for this damping lies in the nature of the resonance phenomenon. In order to fall into resonance, the oblique waves have to assume the phase speed of the two-dimensional primary wave and a certain phase difference between the primary and the secondary wave is required. The phase velocity for intermediate amplitudes is given in figure 12(*b*). In the case of the smallest amplitude (not shown), the wave speed of the oblique wave is only slightly reduced, as was the amplitude. In the case of the moderately large amplitude, however, the wave speed is significantly reduced (figure 12*b*): the wave is slowed down in order to fall into resonance with the primary

https://doi.org/10.1017/jfm.2014.266 Published online by Cambridge University Press

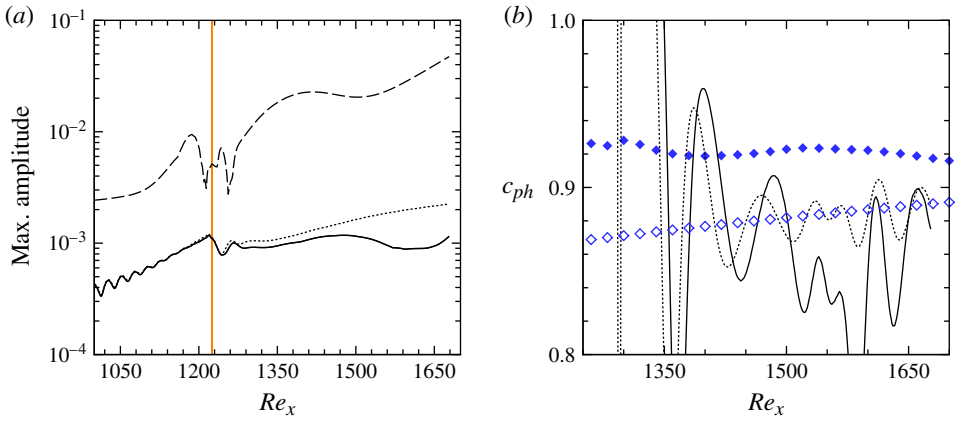


FIGURE 12. (Colour online) (*a*) Same as figure 10(*a*), but for $A_{(1,0)} = 0.0039$. (*b*) Same as figure 11, but for $A_{(1,0)} = 0.0039$.

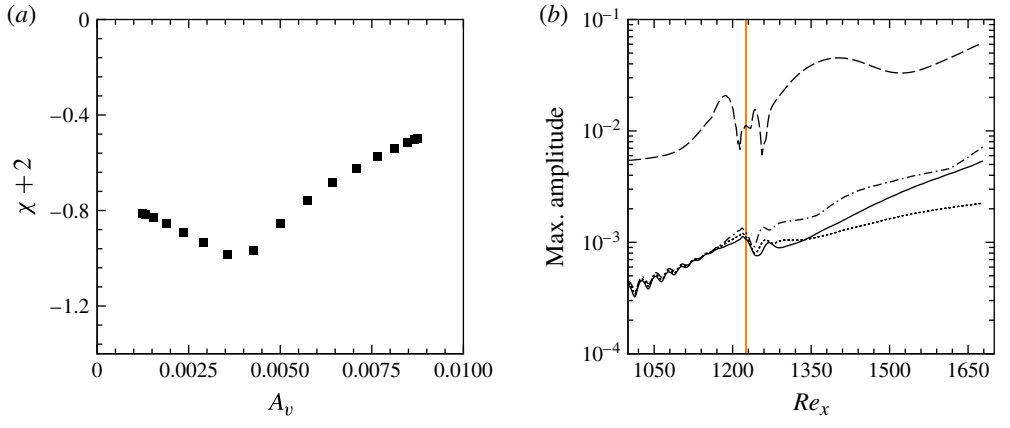


FIGURE 13. (Colour online) (*a*) Response curve for subharmonic secondary waves similar to case *S*, but with varying amplitude of the primary wave. Depicted is χ at $Re_x = 1550$ for a roughness height $h_R = 0.125$ as a function of primary amplitude. (*b*) Same as figure 10(*a*), but showing results for two different values of the phase difference at the location of their respective disturbance strip: $\Delta\Phi = 0$ (—) and $\Delta\Phi = \pi/2$ (– · –).

wave. This is believed to lead to the damping of the oblique waves seen in figure 12(*a*) (solid line).

All the results for different two-dimensional primary amplitudes $A_v = A_{(1,0)}$ are compiled in figure 13, where the value of an amplitude parameter χ downstream of the roughness is given as a function of primary amplitude. The parameter χ is defined as follows:

$$\chi = \log\left(\hat{u}^{max}_{(1/2,\pm1)}\right). \tag{5.1}$$

5.1.2. *Influence of the phase difference between the primary and the secondary wave*

The way in which the primary and the secondary waves become resonant does not only depend on the amplitude of the primary wave but also on the respective

https://doi.org/10.1017/jfm.2014.266 Published online by Cambridge University Press

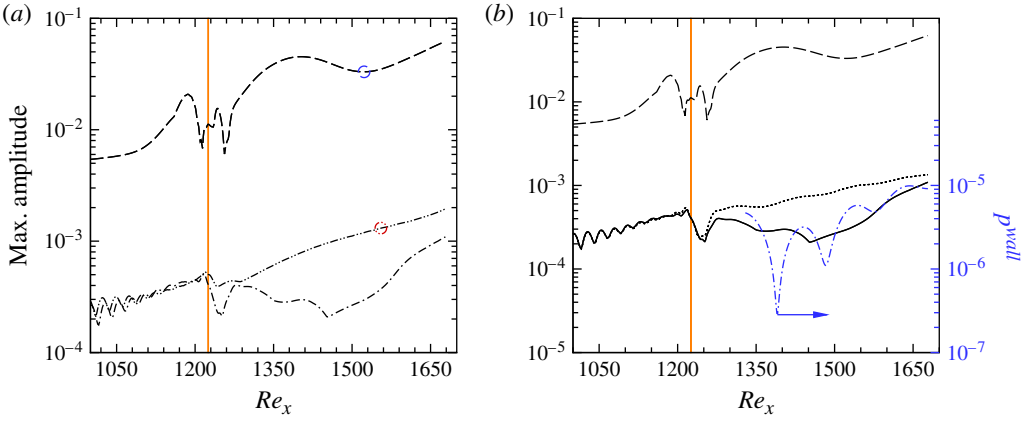


FIGURE 14. (Colour online) (*a*) Similar to figure 10(*a*), but results for two additional spanwise wavenumbers: $\eta = 5.2 = 0.5\eta_0$ (– · –) and $\eta = 15.6 = 1.5\eta_0$ (– · ·). The circles correspond to the local minimum for mode (1, 0) (upper circle) and inflection point for mode (1/2, 3/2) (lower circle). (*b*) Same as figure 10(*a*), but for a spanwise wavenumber $\eta = 5.2$.

phase differences. This is illustrated in figure 13(*b*), where results for two different phase relations are given, set via the phase in the forcing strip, i.e. $\Phi_{0,primary} = 0$ and $\Phi_{0,secondary} = -\pi/2$ or 0 in (2.5). A difference between the amplification rates should not occur far downstream of the roughness once the two waves have gone into resonance. However, this state has not been reached yet for the streamwise length of the domain considered here owing to moderate secondary amplification rates. Still, the difference in amplitude at the largest Re_x remains small. The observation that the overall growth is not much stronger in the case with $\Delta\Phi = \pi/2$, but that the growth rate varies more strongly in the streamwise direction for $\Delta\Phi = \pi/2$ than for $\Delta\Phi = 0$ indicates the occurrence of a beating phenomenon. For this case the phase speed based on p^{wall} was below the linear one for $Re_x \in [1400, 1650]$ (not shown).

5.1.3. *Influence of the spanwise wavenumber*

The spanwise wavenumber considered previously, $\eta = 10.4$, lies in the range of the most amplified wavenumbers for a frequency $F = 0.5 \times 10^{-4}$ for the present case according to linear stability theory (see the line in figure 4*a*). This is confirmed when comparing figure 14(*a*) and figure 13(*b*) in the region upstream of the roughness, where effects of secondary instability are still weak. We observe in this region that the slope of the curves, and hence the amplification rate, for $(h, k) = (1/2, \pm 1/2)$ and $(h, k) = (1/2, \pm 3/2)$ are slightly smaller than the one for $(h, k) = (1/2, \pm 1)$, respectively. Once we observe the onset of secondary growth ($Re_x > 1300$ in the case with $\eta = 15.6$ and $Re_x > 1450$ in the case with $\eta = 5.2$), the secondary amplification rate downstream of the roughness is much stronger for a disturbance with a smaller spanwise wavenumber (the case with $(h, k) = (1/2, \pm 1/2)$, figure 14*b*). However, due to the preceding damping for this low wavenumber, the maximum amplitude is still reached for $|k| = 1$. While we could observe the onset of secondary growth for $\eta = 5.2$ (figure 14*b*), Eissler & Bestek (1996) did not detect any resonant growth for comparable amplitudes of the primary wave for a spanwise wavenumber of $\eta = 6$.

Interestingly, only the case with large spanwise wavenumber ($\eta = 15.6$) does clearly show an influence of the transient growth region for the primary wave immediately

https://doi.org/10.1017/jfm.2014.266 Published online by Cambridge University Press

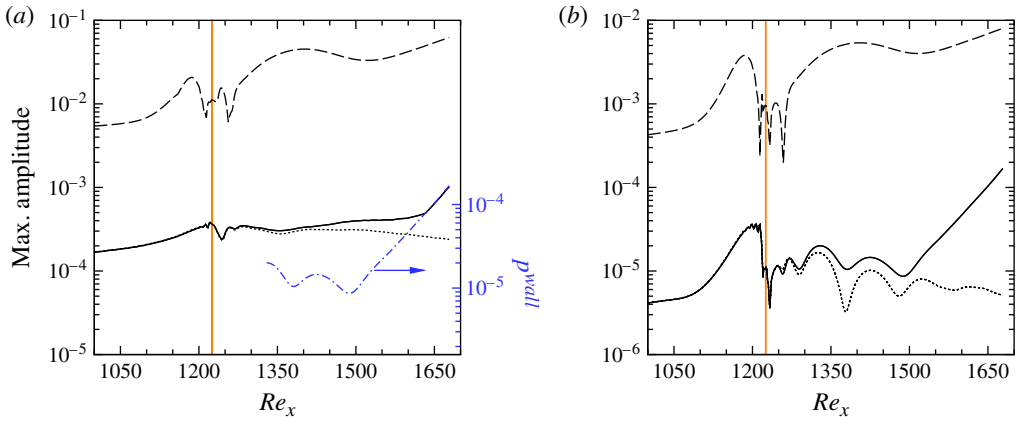


FIGURE 15. (Colour online) Amplitudes $\hat{a}_{(h,k)}$ for $h_R = 0.125$ and different modes (h, k) for a phase difference $\Delta\Phi = \pi/2$. Case F $(1, 0)$ (– –), case F $(1, \pm1)$ (—), case *LIN3D-F* $(1, \pm1)$ $(\cdots)$. (*a*) $\hat{a} = \hat{u}^{max}$ and (*b*) $\hat{a} = \hat{p}^{wall}$. The centre of the roughness is marked by a vertical line. In (*a*), the wall pressure for case F $(1, \pm1)$ is also given for reference with the scale adjusted (– · –), $\eta = 10.4$.

downstream of the roughness: the slope of the curve for mode $(1/2, 3/2)$ correlates well with the amplitude of mode $(1, 0)$, and the former curve possesses an inflection point approximately at the streamwise location where the former reaches a local minimum (compare the streamwise location of the circles in figure 14).

5.2. *Weakly nonlinear results for fundamental secondary waves*

The case of fundamental resonance will be considered next. Eissler & Bestek (1996) investigated the fundamental resonance for a very similar spanwise wavenumber of $\eta = 11.0$ for the same frequency of the primary wave ($F = 10^{-4}$) as considered here, again without a roughness. For their two largest primary amplitudes (their cases F2 and F3) they observed resonant nonlinear growth of the three-dimensional wave. However, even in the case with the largest amplitude of the primary wave, in their cases, did the amplitude of the oblique waves barely exceed values observed further upstream in the disturbance strip due to a long streamwise decay prior to the onset of resonance.

For a flat-plate boundary layer with the same amplitude of the primary wave, we have observed the same growth rate of the secondary wave as Eissler & Bestek (1996) (their case F3), as has already been shown in § 2.5. With roughness, a deviation of amplitudes from the linear behaviour starts almost immediately downstream of the roughness, at $Re_x \approx 1300$ (figure 15). However, strong growth sets in only at $Re_x \approx 1500$, and it is first seen in the pressure amplitudes (figure 15*b*). For $Re_x > 1625$ the amplitude curve of the pressure and the streamwise velocity exhibit the same slopes (figure 15*a*).

Figure 16(*b*) confirms that the onset of strong growth is due to a resonance. For $Re_x > 1500$, the phase velocity of the fundamental oblique waves (solid line in the figure) matches the one of the two-dimensional primary wave as predicted from LST. In the absence of fundamental resonance, the phase velocity is seen to strongly oscillate downstream of the roughness instead (dotted line in the figure). Strong growth is also seen for mode $(0, 1)$ as would be expected for fundamental resonance.

https://doi.org/10.1017/jfm.2014.266 Published online by Cambridge University Press

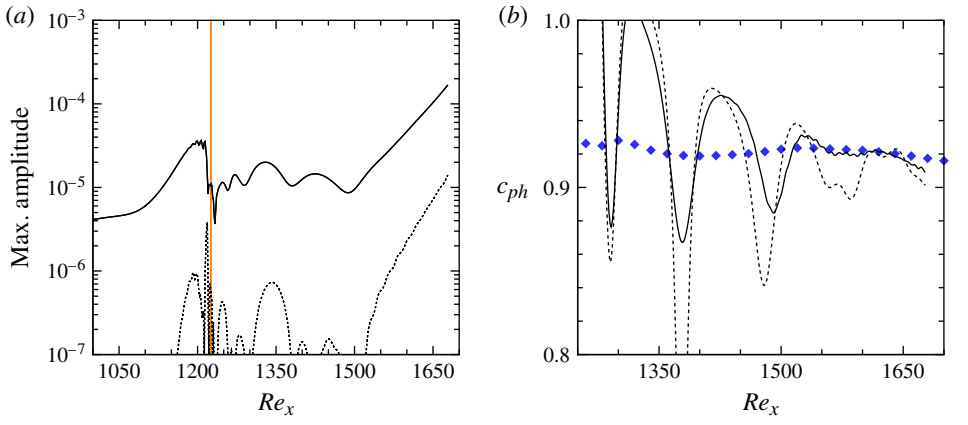


FIGURE 16. (Colour online) (*a*) Amplitudes $\hat{a}_{(h,k)}$ for $h_R = 0.125$ and different modes (h, k) for a phase difference $\Delta\Phi = \pi/2$. Modes (0, 1) $(\cdots)$ and F $(1, \pm 1)$ (—) for case *F*, $\hat{a} = \hat{p}^{wall}$. The centre of the roughness is marked by a vertical line. (*b*) Phase velocity $c_{ph}^{(h,k)}$ for $h_R = 0.125$ from DNS (based on the pressure at $y = 0$) and LST, mode S, for a phase difference $\Delta\Phi = \pi/2$. DNS mode $(h, k) = (1, \pm 1)$ from cases *F* (—) and *LIN3D-F* $(\cdots)$, and LST mode $(h, k) = (1, 0)$ (♦).

However, the slightly different slopes of modes (1, 1) and (0, 1) suggest that the final resonant state has not yet been reached even at the streamwise end of the domain (figure 16*a*).

Again, as in most cases of subharmonic resonance, the local peak in primary amplitude at $Re_x = 1400$ does not cause a local peak in the secondary amplification rate, i.e. a peak in the slope of the amplitude curve for the oblique waves. Instead, resonant growth for $\hat{p}^{wall}$ as well as phase synchronization begin at the location of local minimum in primary amplitude, suggesting that again only the primary mode S contributes to the resonant growth mechanism, and not the transiently amplified mode F.

5.2.1. *Influence of the phase difference between the primary and the secondary wave*

As discussed in § 5.1.2 for the case of subharmonic secondary excitation, the phase difference between the primary and the secondary wave is an important parameter for the onset of resonance for secondary instability. If this difference is not as favourable as in case *F*, no resonant interaction could be observed within the extent of the streamwise domain considered here. Instead, the amplitudes of the pressure and the streamwise velocity exhibit different growth rates (figure 17*a*) and the phase velocity of the oblique wave does not match that of the primary wave (figure 17*b*) even by the streamwise end of the domain, although p^{wall} appears to grow for $Re_x > 1600$ (figure 17*a*).

5.2.2. *Influence of the spanwise wavenumber*

We have varied the spanwise wavenumber in order to see if we observe stronger growth or an earlier onset of growth than in case *F* with $\eta = 10.4$. Corresponding results are depicted in figure 18. For a spanwise wavenumber $\eta = 5.2$, resonance could be observed for $\Delta\Phi = 0$ (figure 18*a*), but not for $\Delta\Phi = \pi/2$ (figure 18*b*). For $\eta = 15.6$,

https://doi.org/10.1017/jfm.2014.266 Published online by Cambridge University Press

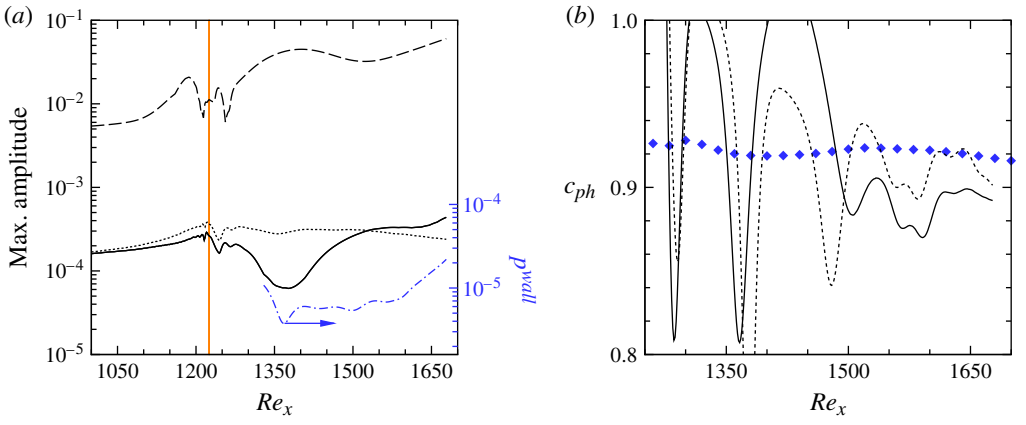


FIGURE 17. (Colour online) (*a*) Same as figure 15(*a*), but for a phase difference $\Delta\Phi = 0$, (*b*) same as figure 16(*b*), but for a phase difference $\Delta\Phi = 0$.

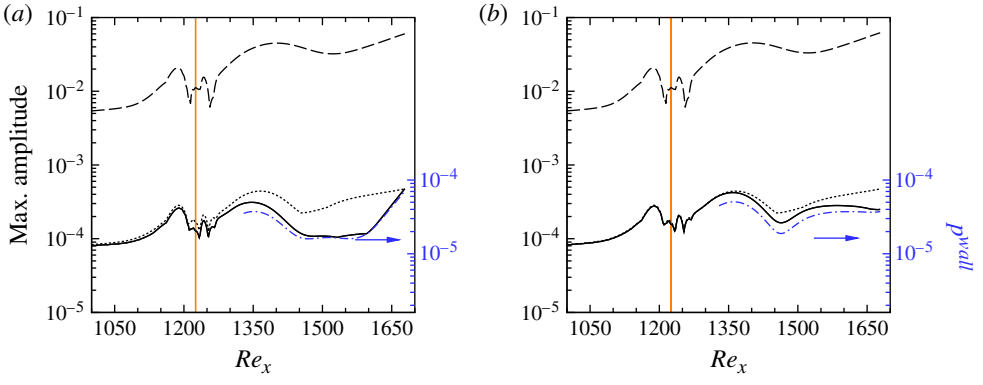


FIGURE 18. (Colour online) Same as figure 15(*a*), but for $\eta = 5.2$ with (*a*) phase difference $\Delta\Phi = 0$ and (*b*) phase difference $\Delta\Phi = \pi/2$.

a common growth rate for u and p^{wall} can be observed for $\Delta\Phi = \pi/2$ (figure 19*b*), but not for $\Delta\Phi = 0$ (figure 19*a*).

Oblique waves with a high spanwise wavenumber ($\eta = 10.4$, 15.6) experience resonance earlier than those with the lower one ($\eta = 5.2$). For $\eta = 15.6$ (figure 19) disturbance growth sets in almost immediately downstream of the roughness, but the shape of the amplitude function continues to change so that amplitude curves for the pressure and the streamwise velocity exhibit different slopes. The growth rate of the pressure assumes roughly constant values for $Re_x > 1550$, but this growth rate is lower than that observed for smaller spanwise wavenumbers. Depending on the phase relation, nonlinear behaviour for the pressure $p^{wall} = p_w$ is seen immediately behind the roughness (figure 19*a*) or further downstream (figure 19*b*). It suggests that for $\eta = 15.6$, the transient growth of the two-dimensional wave behind the roughness, and hence the presence of mode F, has indeed an effect on the secondary instability, unlike in the cases with lower spanwise wavenumbers. Since the onset of secondary instability occurs earlier for $\eta = 10.4$ than for $\eta = 5.2$ and the growth rate for $\eta = 10.4$

https://doi.org/10.1017/jfm.2014.266 Published online by Cambridge University Press

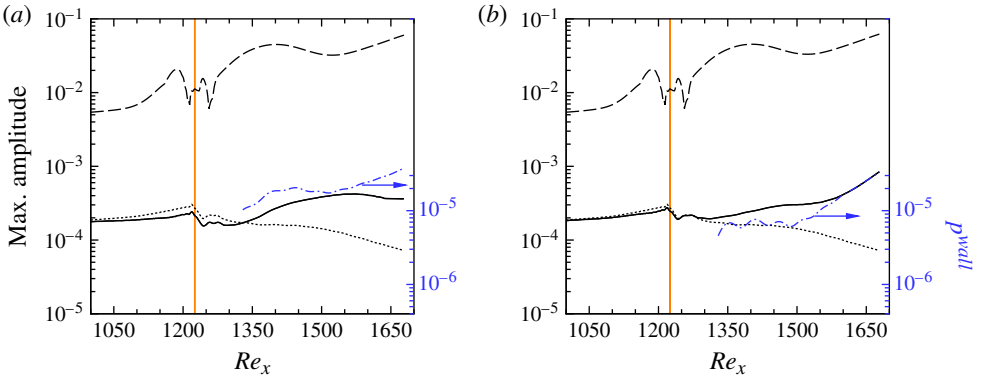


FIGURE 19. (Colour online) Same as figure 15(*a*), but for $\eta = 15.6$ with (*a*) phase difference $\Delta\Phi = 0$ and (*b*) phase difference $\Delta\Phi = \pi/2$.

is larger than that for $\eta = 15.6$, a perturbation with $\eta = 10.4$ achieves the highest gain in amplitude at the end of the domain considered here.

5.3. *Strongly nonlinear stage for subharmonic waves*

In § 5.1, results for case *S* with forcing of a large-amplitude two-dimensional wave but small-amplitude oblique waves have been reported. Now, results for forcing a large-amplitude two-dimensional wave and large-amplitude oblique waves, case *SB*, shall be compared with these earlier results. Figure 20 compares respective results for the most important modes involved. In figure 20(*a*) it can be seen that the amplification of mode (1, 0) is further reduced for $Re_x > 1400$, so that this mode does not grow anymore downstream of $Re_x \approx 1500$. The streak mode (0, 2), however, is hardly affected at all. In case *SB*, this streak mode is the largest perturbation overall in the flow downstream of $Re_x \approx 1500$, and it may therefore be responsible for the reduced growth of the two-dimensional wave mode (1, 0).

As a result of a smaller amplitude of mode (1, 0), the secondary amplification rate of the oblique waves, modes (0.5, $\pm$1), is reduced for $Re_x > 1400$ compared to the results of § 5.1, as can be seen in figure 20(*b*). The weakly nonlinear growth region hence extends up to $Re_x \approx 1400$, followed by a region of strongly nonlinear behaviour downstream of it. In the latter region, the amplitude of modes (0.5, $\pm$1) is almost reduced back to the level observed for purely linear amplification.

6. Conclusions

The nonlinear evolution of disturbances in a Mach 4.8 flat-plate boundary layer with a two-dimensional roughness element has been investigated. Previous simulations have showed that the two-dimensional roughness acts as an amplifier for convective two-dimensional disturbances within a certain frequency band. It elevates the amplitude of mode S to a larger level far downstream compared to the case without roughness. Hence, the amplitude of a two-dimensional wave is shifted to larger values. Moreover, a local peak in amplitude is observed immediately downstream of the roughness due to transient growth caused by the superposition of modes S and F. These observations indicate that the presence of a two-dimensional roughness creates favourable conditions for the occurrence of secondary instability in the presence

https://doi.org/10.1017/jfm.2014.266 Published online by Cambridge University Press

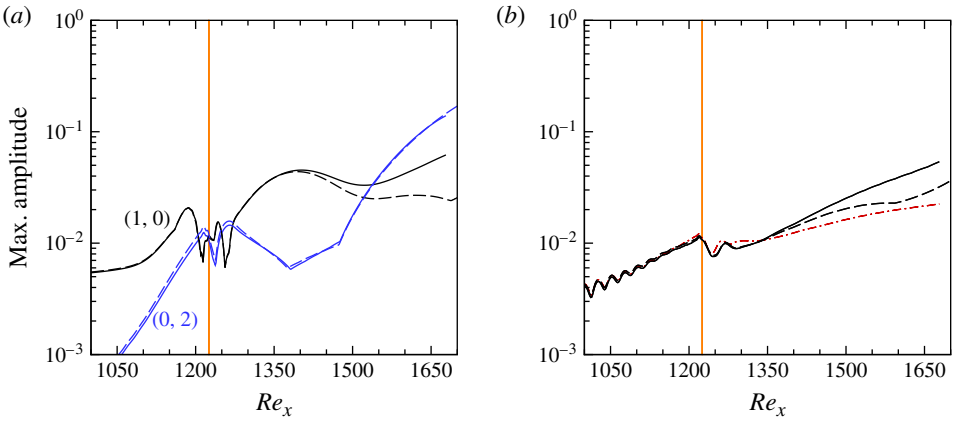


FIGURE 20. (Colour online) Amplitude $\hat{u}^{max}_{(h,k)}$ for $h_R = 0.125$ for two different forcing amplitudes of the oblique waves $A_{(0.5,\pm1)} = 2.5 \times 10^{-4}$ (—) and $A_{(0.5,\pm1)} = 2.5 \times 10^{-3}$ (– –): (*a*) mode (1, 0) and mode (0, 2) as labelled in the figure, and (*b*) modes $(0.5, \pm1)$. The vertical lines mark the centre location of the roughness. The dash-dotted line in (*b*) corresponds to linear amplification of the oblique wave modes $(0.5, \pm1)$. Small-amplitude results for modes (0, 2) and $(0.5, \pm1)$ have been scaled in order to match upstream of the roughness.

of a large-amplitude two-dimensional wave. This secondary instability has been investigated in detail, including parameters such as the amplitude of the primary wave, the phase difference between the primary and the secondary waves, and the spanwise wavenumber of the secondary wave. In our investigation, we have chosen all governing parameters such that the roughness would potentially influence the laminar–turbulent transition process directly. Cases for which the onset of secondary instability or a fully resonant state would occur only far behind the roughness were outside the scope of the present investigation.

It is found that for the case of subharmonic resonance, the combined effect of primary and secondary growth in the presence of the roughness favours a spanwise wavenumber for which linear growth is largest as well. For fundamental resonance, essentially the same spanwise wavenumber was seen to exhibit largest amplitude growth over the streamwise domain considered here. Although the variation of spanwise wavenumbers was not extensive in our investigation, our results indicate that those wavenumbers that already exhibit the strongest linear growth may be important if secondary growth is considered in addition to primary growth.

The nonlinear growth rates for fundamental resonance are larger than those for subharmonic resonance. However, the amplitude for subharmonic perturbations was found to be larger at the streamwise end of the domain considered here due to larger linear amplification, which precedes the nonlinear amplification.

The roughness-induced transient disturbance growth of the primary wave immediately downstream of the roughness does not lead to a local increase in secondary amplification for almost all cases considered here. This observation suggests that mode S is mainly responsible for triggering secondary instability. This hypothesis requires further analysis, and it may be useful to consider a technique such as the multi-mode decomposition by Tumin (2007) in order to shed light on this matter. Overall, secondary growth rates are only moderately large. Moreover, when the

https://doi.org/10.1017/jfm.2014.266 Published online by Cambridge University Press

secondary amplitude reaches sufficiently large amplitudes, this growth rate is further reduced due to the feedback of the secondary disturbances to the primary wave.

Variations in roughness dimensions were previously found to mainly influence the amplitude of the two-dimensional wave, which acts as the primary wave in our study. Since we investigated the effect of the amplitude of the primary wave in our study, our results should also hold when varying roughness dimensions. Changing these dimensions was previously found to influence transient growth, but this growth is seen here to have a minor effect only. Nevertheless, parametric variations of roughness dimensions should be carried out in the future in order to confirm theses hypotheses.

A resonance with all its typical characteristics does not set in very rapidly behind the roughness. The oblique breakdown scenario should therefore be checked to see whether it provides a faster route to turbulence than the secondary instability investigated here.

Acknowledgements

Financial support from the National Aeronautics and Space Administration (NASA) under award No. NNX07AC29A is gratefully acknowledged. We are grateful to S. Lele, Stanford University, for providing the finite-difference code, which served as a basis for the DNS code used in this work.

REFERENCES

ADAMS, N. A. & KLEISER, L. 1996 Subharmonic transition to turbulence in a flat-plate boundary layer at Mach number 4.5. *J. Fluid Mech.* **317**, 301–335.

BOUNTIN, D., SHIPLYUK, A. & MASLOV, A. 2008 Evolution of nonlinear processes in a hypersonic boundary layer on a sharp cone. *J. Fluid Mech.* **611**, 427–442.

DUAN, L., WANG, X. & ZHONG, X. 2013 Stabilization of a Mach 5.92 boundary layer by two-dimensional finite-height roughness. *AIAA J.* **51** (1), 266–270.

EISSLER, W. & BESTEK, H. 1996 Spatial numerical simulations of linear and weakly nonlinear wave instabilities in supersonic boundary layers. *Theor. Comput. Fluid Dyn.* **8** (3), 219–235.

FEDOROV, A. V. 2011 Transition and stability of high-speed boundary layers. *Annu. Rev. Fluid Mech.* **43**, 79–95.

FUJII, K. 2006 Experiment of the two-dimensional roughness effect on hypersonic boundary-layer transition. *J. Spacecr. Rockets* **43** (4), 731–738.

HEITMANN, D. & RADESPIEL, R. 2013 Simulations of boundary-layer response to laser-generated disturbances at Mach 6. *J. Spacecr. Rockets* **50** (2), 305–316.

HERBERT, T. 1988 Secondary instability of boundary layers. *Annu. Rev. Fluid Mech.* **20**, 487–526.

KENDALL, J. M. 1975 Wind tunnel experiments relating to supersonic and hypersonic boundary-layer transition. *AIAA J.* **13** (3), 290–299.

KIMMEL, R. L. & POGGIE, J. 1997 Disturbance evolution and breakdown to turbulence in a hypersonic boundary layer – ensemble-averaged structure. *AIAA Paper* 1997-555.

LIFSHITZ, Y., DEGANI, D. & TUMIN, A. 2012 Study of discrete modes branching in high-speed boundary layers. *AIAA J.* **50** (10), 2202–2210.

MA, Y. & ZHONG, X. 2003 Receptivity of a supersonic boundary layer over a flat plate. Part 1. Wave structures and interactions. *J. Fluid Mech.* **488**, 31–78.

MACK, L. M. 1969 Boundary layer stability theory. *Tech. Rep.* JPL-900-277-REV-A; *NASA-CR*-131501. Jet Propulsion Laboratory, NASA.

MARXEN, O., IACCARINO, G. & SHAQFEH, E.S.G. 2010 Disturbance evolution in a Mach 4.8 boundary layer with two-dimensional roughness-induced separation and shock. *J. Fluid Mech.* **648**, 435–469.

https://doi.org/10.1017/jfm.2014.266 Published online by Cambridge University Press

MARXEN, O., MAGIN, T., IACCARINO, G. & SHAQFEH, E.S.G. 2011 A high-order numerical method to study hypersonic boundary-layer instability including high-temperature gas effects. *Phys. Fluids* **23**, 084108.

MAYER, C. S. J., VON TERZI, D. A. & FASEL, H. F. 2011*a* Direct numerical simulation of complete transition to turbulence via oblique breakdown at Mach 3. *J. Fluid Mech.* **674**, 5–42.

MAYER, C. S. J., WERNZ, S. & FASEL, H. F. 2011*b* Numerical investigation of the nonlinear transition regime in a Mach 2 boundary layer. *J. Fluid Mech.* **668**, 113–149.

NAGARAJAN, S., LELE, S. K. & FERZIGER, J. H. 2003 A robust high-order method for large eddy simulation. *J. Comput. Phys.* **191**, 392–419.

NG, L. L. & ERLEBACHER, G. 1992 Secondary instabilities in compressible boundary layers. *Phys. Fluids* A **4** (4), 710–726.

PAGELLA, A., RIST, U. & WAGNER, S. 2002 Numerical investigations of small-amplitude disturbances in a boundary layer with impinging shock wave at $Ma = 4.8$. *Phys. Fluids* **14** (7), 2088–2101.

RESHOTKO, E. & TUMIN, A. 2004 Role of transient growth in roughness-induced transition. *AIAA J.* **42** (4), 766–770.

TUMIN, A. 2007 Three-dimensional spatial normal modes in compressible boundary layers. *J. Fluid Mech.* **586**, 295–322.

VAN DRIEST, E. R. & BLUMER, C. B. 1968 Boundary-layer transition at supersonic speeds – roughness effects with heat transfer. *AIAA J.* **6** (4), 603–607.

https://doi.org/10.1017/jfm.2014.266 Published online by Cambridge University Press